Journal of Alloys and Compounds 942 (2023) 168953

Contents lists available at ScienceDirect

Journal of Alloys and Compounds

journal homepage: www.elsevier.com/locate/jalcom

Research Article

Corrosion resistance of calcium hexaaluminate insulating firebrick for synthesising ternary lithium-ion battery cathode materials

Bo Yin [a,d], Yuanbing Li [a,b,*], Shun Wang [c], Yifeng Zheng [c,**]

[a] The State Key Laboratory of Refractories and Metallurgy, Wuhan University of Science and Technology, 430081 Wuhan, PR China
[b] National-provincial Joint Engineering Research Center of High Temperature Materials and Lining Technology, Wuhan University of Science and Technology, 430081 Wuhan, PR China
[c] College of Materials Science and Engineering, Nanjing Tech University, 211816 Nanjing, PR China
[d] Yixing Morgan Thermal Ceramics Co., Ltd, 214222 Yixing, PR China

ARTICLE INFO

Article history:
Received 13 December 2022
Received in revised form 12 January 2023
Accepted 18 January 2023
Available online 19 January 2023

Keywords:
Insulating refractory
Corrosion resistance
Lithium-ion battery cathode materials
Mullite
CA_6

ABSTRACT

The widespread use of ternary lithium-ion battery cathode $Li(Ni_xCo_yMn_{1-x-y})O_2$ (LNCM) materials in energy storage equipment has resulted in an increase in the demand for insulating refractory of roller kiln. However, the severe corrosion during LNCM calcination will result in desquamate and damage of the insulating refractory. In this study, the corrosion resistance of bubble alumina brick (bubble alumina), mullite and CA_6 (calcium hexaaluminate) insulating refractories was thoroughly investigated. This study combined the laboratory scale experiments on the interfacial reaction and after life cycle analysis on industrial insulating refractory to investigate the interactions between the insulating refractories and LNCM precursor mixture powders after the calcination temperature of 950 °C for 10 h and the corrosion behaviour of the LNCM precursor to different insulating fire bricks after the heat treatment temperature of 950 °C for 10 h every time and repeated 10 times according to the actual LNCM preparation system. The phase composition and microstructure of the three insulating refractories before and after corrosion were characterised to obtain a comprehensive understanding of the corrosion mechanism and behaviour. Results showed that the CA_6 has excellent corrosion resistance and has the potential to be used in the lithium battery industry.

1. Introduction

Energy storage equipment is essential in modern social life [1,2]. Rechargeable lithium-ion batteries (LIB) are widely used in electronic portable devices, plug-in hybrid electric vehicles (PHEVs), electric vehicles (EVs), wearable electronics and medical devices due to their high capacity [3–5]. In the LIB technology, the cathode material is the key to determining the cost and energy density of the battery. The cathode material is distinguished by its low price, easy production, environmental friendliness and good electrochemical performance. Ni-rich ternary cathode materials $Li(Ni_xCo_yMn_{1-x-y})O_2$ (LNCM, $x \geq 0.8$) have great application potential in LIB due to its advantages of high capacity, long life cycle, low cost and excellent structural stability at high temperatures [6,7].

In the industrial production, LNCM materials are mainly prepared through high-temperature solid-state reactions because of the simple equipment and production process [8,9]. LNCM materials are calcined in a roller kiln, and the insulating refractory is the mainly component of the roller kiln [10–12]. Bubble alumina brick (bubble alumina) is extensively used as an insulating refractory for the high-temperature equipment due to its high melting point, high refractory and suitability for oxidation and reduction atmospheres at high temperatures [13,14]. This material is typically applied in a metallurgical reactor, a coal gasifier and a chemical reactor in the steel industry [15–17]. Mullite ($3Al_2O_3{\cdot}2SiO_2$) is the only stable phase in the Al_2O_3–SiO_2 system, has the advantages of high density and purity, high structural strength and low creep rate at high temperature, low thermal expansion rate, strong resistance to chemical erosion and thermal shock [18]. Mullite insulating fire brick is typically used to prepare LNCM materials during the synthesis process, whilst the life cycle of mullite material is limited due to the harsh application environment [19]. Calcium hexaaluminate (CA_6) is a high-temperature calcium aluminate phase with the highest Al_2O_3 content in the CaO–Al_2O_3 system [20,21]. CA_6 has high

* Corresponding author at: The State Key Laboratory of Refractories and Metallurgy, Wuhan University of Science and Technology, 430081 Wuhan, PR China.
** Corresponding author.
E-mail addresses: lybref2002@126.com (Y. Li), zhengyifeng@njtech.edu.cn (Y. Zheng).

https://doi.org/10.1016/j.jallcom.2023.168953
0925-8388/

refractoriness, excellent chemical stability, good CO erosion resistance, low thermal expansion coefficient and other excellent characteristics, and it has been used in the chemical industry, aluminium smelting and backing materials. However, fewer studies have been conducted on the CA_6 insulating refractory/fire brick for LIB cathode material synthesis.

In LIB cathode materials, the lithium source of the nickel-rich LNCM materials is more aggressive than that of other conventional cathode materials [22]. LiOH is the lithium source used in high-nickel LNCM materials. During calcinations, the corrosion of vapours from the LNCM material precursors causes desquamate and damage of the insulating refractory, resulting in the contamination of LNCM materials and normal production operation [23–25]. Accordingly, the corrosion mechanism of insulating refractory for synthesising LNCM cathode materials is indispensable to control and improve the purity of the LNCM materials and the life of the insulating refractory. Currently, several studies mainly focus on the interactions of LNCM and saggar materials [19,22,26]. However, studies on LNCM and insulating refractory are limited. In our previous study, we have investigated the interaction behaviours of mullite insulating refractory with LNCM materials between 1000 °C and 1300 °C [27]. The result showed that the insulating refractory with excellent resistance to alkali corrosion should be selected for LNCM preparation. However, the study used more severe experimental conditions to accelerate the degradation of the tested materials, and the test temperatures were above 1000 °C. Consequently, the study cannot actually simulate the real LNCM production situation.

No study has been conducted on the corrosion mechanisms of different insulating refractories for the preparation of LNCM materials. Different insulating refractories may have varying corrosion behaviours during the LNCM calcination due to their distinct chemical compositions and structures. Understanding the corrosion resistance behaviour is also crucial for selecting the right insulating refractory. Currently, the nickel-rich ternary cathode material is typically heat-treated at 800–950 °C for 10–20 h [28–30]. Consequently, bubble alumina, mullite and CA_6 insulating refractories were selected under the actual LNCM material calcination conditions to compare the corrosion mechanism and behaviour for LNCM preparation.

In this work, the comparison of corrosion resistance for bubble alumina, mullite and CA_6 insulating refractories were investigated. To fully identify and understand the occurring corrosion mechanism and corrosion behaviour, this study combined the laboratory scale experiments on the interfacial reaction and after life cycle analysis on industrial insulating refractories to investigate the interactions between the insulating refractories and LNCM precursor mixture powders and the corrosion behaviour of LNCM precursor to different insulating fire bricks. The interactions between insulating refractories and LNCM materials were analysed and compared to investigate the corrosion mechanism according to the actual LNCM preparation system. The heat treatment temperature of 950 °C for 10 h every time was selected and repeated 10 times (until corrosion was observed on a macro scale in the industrial insulating fire brick) to investigate the corrosion behaviour.

2. Experimental

2.1. Material preparation

The bubble alumina, mullite and CA_6 insulating refractories were supplied by Yixing Morgan Thermal Ceramics Co., Ltd, China. The chemical composition and product introduction of the three insulating refractories are listed in Tables 1 and 2, respectively. The LNCM precursor mixture powders were prepared by mixing commercially available $Ni_{0.8}Co_{0.1}Mn_{0.1}(OH)_2$ (supplied by Haian Zhichuan Battery Material Technology Co., Ltd, China, ≥99.0 wt% purity) and $LiOH{\cdot}H_2O$ (Shanghai Aladdin Biochemical Technology Co., Ltd, anhydrous, ≥99.0 wt% purity) powders at a mole ratio of 1:1.05.

Table 1
Chemical composition of the three insulating refractories.

Chemical composition (wt%)	Bubble alumina	Mullite	CA_6
Al_2O_3	98.13	73.41	90.55
SiO_2	0.92	23.69	0.240
CaO	0.157	0.151	8.33
Na_2O	0.584	0.324	0.398
K_2O	0.07	0.516	–
Fe_2O_3	0.04	0.442	0.05
TiO_2	0.03	0.229	0.01
MgO	–	0.043	0.077
ZrO_2	–	0.307	–

Table 2
Product introduction of the three insulating fire bricks.

		Unit	Bubble alumina	Mullite	CA_6
Bulk density		g/cm^3	1.45	0.97	0.97
Cold crushing strength		MPa	10	3.5	3.5
Cold modulus of rupture		MPa	3.5	2.0	2.0
Permanent linear change on heating		% (12 h at 1570 °C)	−0.2	−0.3	−0.21
Thermal conductivity (at mean temperature)	400 °C	W/m.K	0.75	0.35	0.23
	800 °C	W/m.K	0.9	0.39	0.27

Preparation of interfacial reaction test samples: all the insulating refractories were firstly crushed and screened (100 mesh) to accurately analyse the corrosion reaction between the insulating refractories and LNCM materials. The insulating refractory powders and LNCM precursor mixture powders were then mixed at a weight ratio of 1:1 and placed in a polyurethane ball mill jar. Zirconium balls (4–6 mm in diameter) were added to the jar, the ball/powder weight ratio was 2:1, and the jar was sealed and ball milled at a speed of 30 r/min for 4 h. Subsequently, 6 wt% polyvinyl alcohol (PVA, 8 % concentration) was added to the mixed powder and stirred well. The mixture was uniaxially compacted to cylinders (diameter=25 mm, height=8 mm, weight=15 g) at a pressure of 50 MPa. The obtained cylindrical samples were placed in the furnace and heat treated at 950 °C for 10 h (Fig. 1a). After the materials were reduced to room temperature, the phase composition and microstructure were analysed with an X-ray diffractometer (XRD) and scanning electron microscope (SEM), respectively.

Preparation of corrosion test samples: a cube-shaped insulating refractory (industrial insulating fire brick) with 50 mm sides was cut from the industrial sample brick to study the corrosion behaviour of an insulating refractory during the ternary cathode material synthesis, preserving as much of the original surface as possible. A hole with a diameter of 22 mm and a depth of 25 mm is drilled in the centre of one surface of the sample. Moreover, a 50 mm × 50 mm× 6 mm cover was cut for each sample. Then, the corrosion test of the bubble alumina, mullite and CA_6 insulating refractories was carried out. Approximately 8 g LNCM precursor mixture powders were placed into different cubes and covered. Thereafter, the insulating refractory cubes with LNCM mixed powders were heat treated for 10 h in a muffle furnace at 950 ℃ under an oxidising atmosphere before furnace cooling. The above-mentioned corrosion test was repeated 10 times (Fig. 1b). After the corrosion test, the appearance of the longitudinal section after cutting the cube was examined to analyse the bottom morphology and measure the thickness of the reaction layer. The macroscopic and microscopic analysis of the samples was carried out.

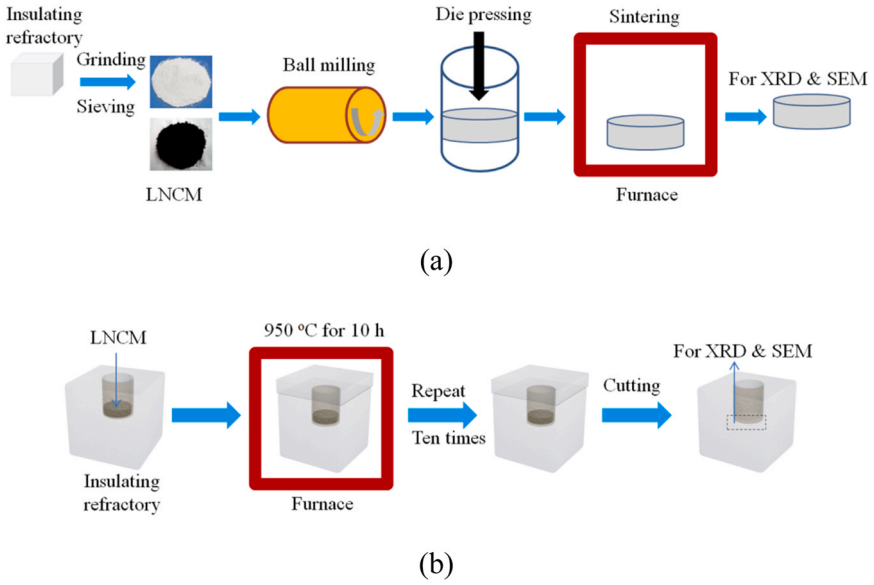

Fig. 1. Sample for corrosion testing: (a) preparation of interfacial reaction test samples and (b) preparation of corrosion test samples.

2.2. Characterisation methods

The crystalline phase compositions were investigated by XRD with an ARL X'TRA diffractometer with Cu Kα radiation. The diffractometer was operated at 40 kV and 35 mA in the 2θ range of 20°–80° with a step size of 0.02°. The microstructures were analysed with an SEM (JSM-5900, JEOL, Japan) system coupled with an energy dispersive X-ray spectroscopy (EDS) system. A pore size distribution was measured by using mercury porosimetry (AutoPore IV 9500, Micromeritics).

3. Results and discussion

3.1. Characterisation before corrosion

The phase compositions of the three insulating refractory are illustrated in Fig. 2. The samples show sharp diffraction peaks, indicating the well-developed crystals of the three insulating refractories. The phase of the bubble alumina sample is only alumina. The crystal composition of the mullite sample is mostly mullite and alumina, which is in consistent with previous studies [27]. The main

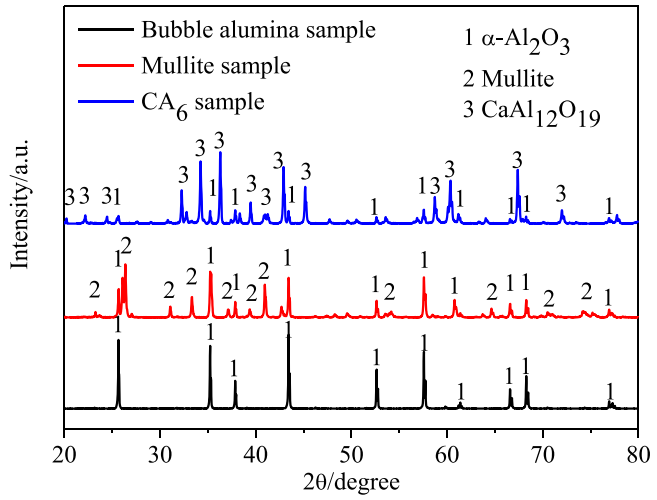

Fig. 2. XRD patterns of the three insulating refractories.

peaks of the CA_6 sample are assigned to the $CaAl_{12}O_{19}$ phase, and a small amount of alumina phase is observed. Given that the sufficient alumina source promoted CA_6 generation through a solid-state reaction at the interface and impeded the continuous reaction, a small amount of alumina was present in the CA_6 insulating refractory [31]. However, the peak intensities of alumina in the CA_6 sample sharply decrease compared with those in the bubble alumina and mullite samples.

Fig. 3 displays the SEM images of the three insulating refractories. The distribution of grain size for the bubble alumina sample is relatively uniform, and certain pores are present between the grain and the formation different sizes of intermittent pores. The microstructure of the mullite sample shows the similar composition and structure. The grains are columnar and the network structure formed by the mullite grains is enclosed. The overall morphology of CA_6 sample is similar, with the majority of plate-like crystals. The stacking of the plate-like grains and their card-house structures can stabilise the open-porous structure. The microstructure of the CA_6 sample is relatively finer than that of the bubble alumina and mullite samples.

Fig. 4 shows the pore size distribution of the three insulating refractories. The pore size of the bubble alumina sample varies from 2 μm to 200 μm, indicating that the pore size distribution range is wide and there are lots of large pores. The pores in the mullite sample are mainly distributed from 5 μm to 70 μm and concentrated at 5 or 70 μm, indicating that the distribution shifts from small to larger pore sizes. The pore size of the CA_6 samples is mainly distributed between 2 μm and 5 μm, indicating that the sample has only small pores, and all the pores concentrated in a small range. The above-mentioned results suggest that the pore size of the CA_6 sample is significantly smaller than that of the bubble alumina and mullite samples.

3.2. Interactions between the insulating refractories and the LNCM powders

The phase evolution of the insulating refractories at the calcination temperature of 950 °C for 10 h is shown in Fig. 5. A comparison of the XRD results before and after the corrosion of the three insulating refractory shows that the chemically reacted with the LCNM precursor is lithium, whilst Ni, Co and Mn do not chemically react with them. This condition arises because only LiOH is volatile

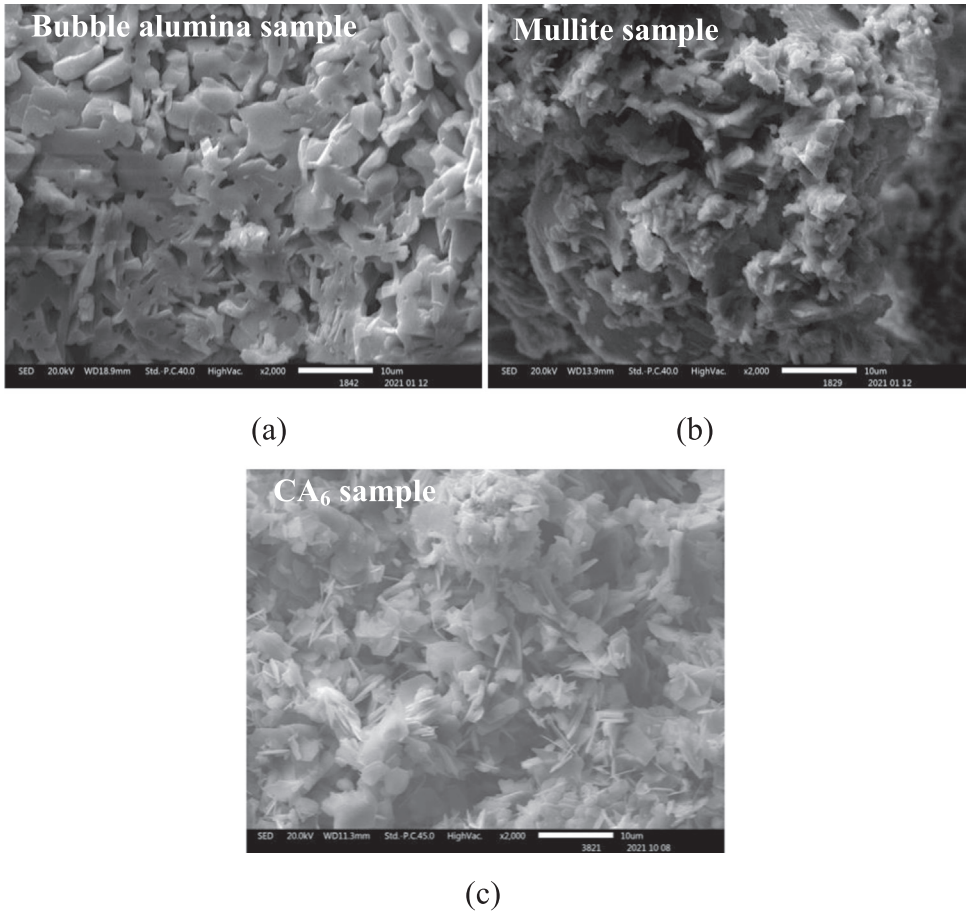

Fig. 3. SEM images of the three insulating refractories: (a) bubble alumina, (b) mullite and (c) CA_6 samples.

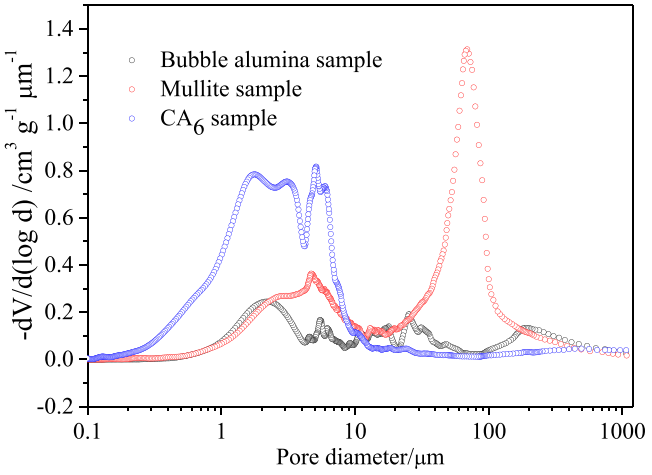

Fig. 4. Pore size distribution of the three insulating refractories.

in the LNCM precursor [27]. Given that the melting and decomposition temperatures of LiOH are 411 °C and 435 °C [32], the corrosion atmosphere from LNCM is LiOH when the temperature is below 435 °C, and the corrosion atmosphere is Li_2O when the temperature is above 435 °C. In Fig. 5, the new phases for all the three samples are $LiAlO_2$ and $Li_xNi_{0.8}Co_{0.1}Mn_{0.1}O_2$ ($x < 1$) after corrosion. This condition is due to all the insulating refractories that contain the alumina (Al_2O_3) phase (Fig. 2), and the observed $LiAlO_2$ should be generated from the following solid state reaction:

$$Al_2O_3 + Li_2O = 2LiAlO_2. \quad (1)$$

Furthermore, partial Li in the LiOH has reacted with Al_2O_3, resulting in less Li content in LiOH, which will combine with $Ni_{0.8}Co_{0.1}Mn_{0.1}(OH)_2$ to synthesise LNCM ternary cathode materials. Consequently, the $Li_xNi_{0.8}Co_{0.1}Mn_{0.1}O_2$ ($x < 1$) phase is detected. Therefore, the main reaction product is $LiAlO_2$ between the different insulating refractories and the LNCM precursor at 950 °C. Furthermore, the peak intensities of $LiAlO_2$ for the CA_6 sample are the weakest amongst the three insulating refractories due to the least amount of alumina in the CA_6 sample (as shown in Fig. 2).

The microstructures of the LNCM precursor-insulating refractory cylinders after heat treatment at 950 °C for 10 h are presented in Fig. 6. The bright white part is the phase formed by the reaction of the LNCM precursor, and the grey portion is the different insulating refractories. In Fig. 6, the LNCM agglomerates and insulating refractory grains of the bubble alumina and mullite samples are significantly larger than those of CA_6 sample. In Figs. 6b and 6d, LNCM reacts with bubble alumina or mullite samples (where the arrows are pointing), the reaction will lead to the formation of cracks. Fig. 7 illustrates the EDS images of the mullite sample. All the elements have diffused from each other, confirming the reaction between mullite and LNCM. However, the LNCM agglomerates and CA_6 grains are separately distributed in the sample, and the interface is clear between them (Fig. 6f), suggesting no obvious reaction between LNCM and CA_6. The XRD characterisations and SEM observations demonstrate that the CA_6 sample is the least reactive with LNCM amongst the three samples, which has good corrosion resistance to the LNCM.

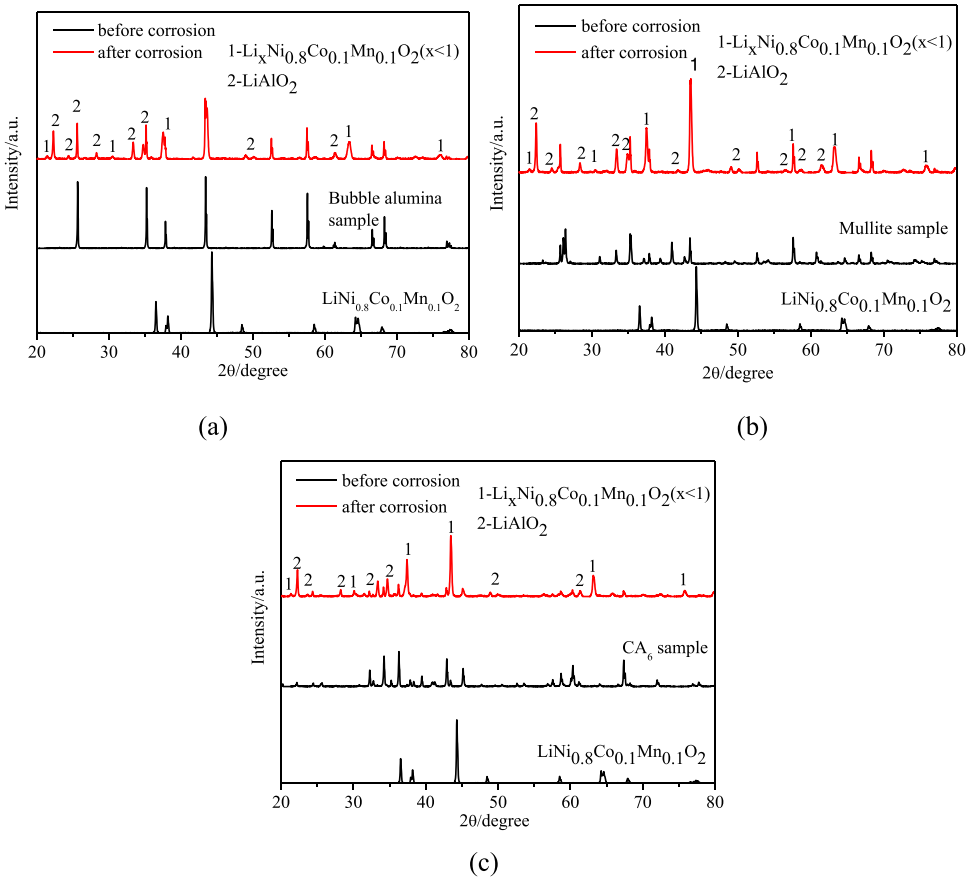

Fig. 5. XRD patterns of the insulating refractories mixed with the LNCM precursor after heat treatments at 950 °C for 10 h: (a) bubble alumina, (b) mullite and (c) CA_6 samples.

3.3. Corrosion resistance results of the different insulating refractories

Fig. 8 shows the macrograph view for the section of the three insulating refractories after 10 times of corrosion. The figures demonstrate that the bubble alumina and mullite samples suffer significant corrosion compared with the uncorroded parts (the outer parts of the sample). In Fig. 8a, many large pores are near the interface of LNCM and bubble alumina sample. The LNCM has seriously corroded into the bubble alumina sample. In Fig. 8b, different coloured layers appear near the interface of the LNCM and mullite sample. In Fig. 8c, the interface of the LNCM and CA_6 sample is relatively clear, no particularly significant corrosion is observed.

The section colour view of the reaction layer at the bottom of the samples is shown in Fig. 9 for further comparison. The corroded depth of the samples is measured using the graph. The corroded depth of the bubble alumina sample is about 3.6 mm, and the number of big pores is decreases with the depth of corrosion. The colour of the corroded layer of the mullite sample changes from black to green to brown with the depth of corrosion. The corroded depth is about 3.1 mm. In particular, the corroded depth of the CA_6 sample is only about 1 mm. Therefore, the bubble alumina and mullite samples were severely corroded by LNCM, and the CA_6 sample was only slightly corroded.

The different areas of the corroded layers for the different insulating refractories further conducted by SEM observation are shown in Fig. 10. Fig. 10A_1–A_4 shows the SEM results of the bubble alumina sample. The microstructure is relatively porous in Fig. 10A_1, indicating that the reaction layer is relatively loose. The microstructures become dense with the depth of corrosion, as shown in Fig. 10A_2 and A_3. During corrosion, the bulk densities of the original sample and the reaction product are different. The bulk density of the new phase $LiAlO_2$ (Fig. 5) is 2.61 g/cm^3 [33], whilst that of the bubble alumina sample is 1.45 g/cm^3 (Table 2). The volume change in the reaction process will result in the loose or even peeling phenomenon of the reaction layer. Meanwhile, the permeability of Li_2O is extremely strong, and it is easy to diffuse into the sample along the pores. The diffusion is accelerated with the increase and persistence of the reaction temperature, and the corrosion reaction continues. The large pores of the bubble alumina sample (Fig. 4) may also facilitate the diffusion. In Fig. 10A_2 and A_3, the particles in the permeable layer are integrated with the matrix, and the edge of the particles is passivated. The new phase generated by the reaction fills the pores, reducing the porosity of the permeable layer. This structure can inhibit the further reaction between Li_2O diffusion and the internal structure to reduce the further damage of corrosion reaction to the insulating refractory. Fig. 10A_4 shows the porous structure, which is consistent with the original brick. In the mullite sample, the reaction layer in direct contact with LNCM is the most loose and porous (Fig. 10B_1). The structure changes from porous (Fig. 10B_2) to dense (Fig. 10B_3) with the depth of corrosion. In Fig. 10B_3, the particles and the matrix are integrated each other, and the large pores (mainly concentrated at 70 μm) of the mullite sample may also promote the penetration of Li_2O, resulting in the densification. The structure is also relatively loose and will easily fall off. Fig. 10B_4 shows the porous structure of the original brick. Overall, the corrosion resistance of mullite is better than that of bubble alumina, which is consistent with the XRD results (Figs. 5a and 5b). However, the corroded depth of the CA_6 sample is only about 1 mm, as shown in Fig. 9c. The microstructure is relatively dense in Fig. 10C_1, and the interface between the particles is relatively clear. The microstructure in Fig. 10C_1 is similar to that of the matrix in Fig. 10C_2. This finding indicates that the CA_6 sample has a good corrosion resistance. This

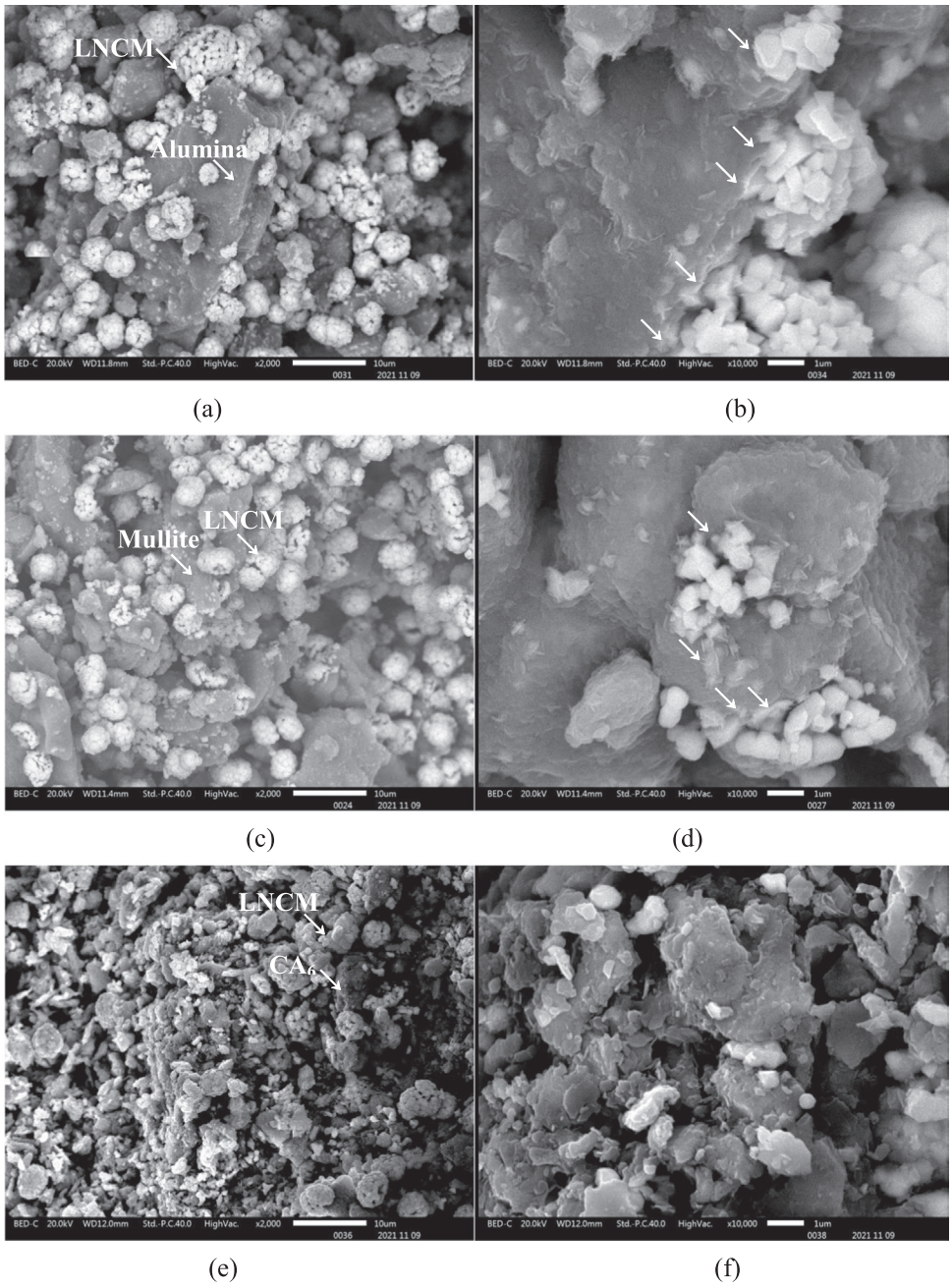

Fig. 6. SEM images between the LCNM precursor and the insulating refractory after heat treatments at 950 °C for 10 h: (a) bubble alumina sample and (b) the enlarged view; (c) mullite sample and (d) the enlarged view; and (e) CA_6 sample and (f) the enlarged view.

phenomenon may be due to two reasons. The first reason is that only minimal reaction occurred between Li_2O and CA_6 (Fig. 5c), indicating that almost no new phases are formed. Another reason is that the small pores of CA_6 (Fig. 4) will inhibit the penetration of Li_2O. A little penetration occurred, and the small pore can obtain a larger specific surface area, resulting in a larger area for the dilution of pollutants and a better corrosion resistance. The above-mentioned results further confirm that the CA_6 sample has the best corrosion resistance amongst the three insulating refractories.

4. Conclusion

The comparison of the corrosion resistance for bubble alumina, mullite and CA_6 insulating refractories used for synthesising LNCM cathode materials were studied. The laboratory scale experiments on the interfacial reaction and after life cycle analysis on industrial insulating refractories were combined. Based on the phase, macro and micro morphology analysis, the conclusion can be drawn:

(1) The main reaction product was $LiAlO_2$ between the insulating refractory and LNCM precursor at 950 °C. The peak intensities of $LiAlO_2$ for the CA_6 sample were the weakest amongst the three insulating refractories. Moreover, LNCM reacted with bubble alumina or mullite samples from the interaction analysis. The reaction will lead to the formation of cracks. However, no obvious reaction occurred between LNCM and CA_6.
(2) The corroded depths of the bubble alumina, mullite and CA_6 insulating fire bricks were about 3.6, 3.1 and 1 mm after the heating treatment at 950 °C for 10 h every time and repeated 10 times, respectively. The bubble alumina and mullite samples

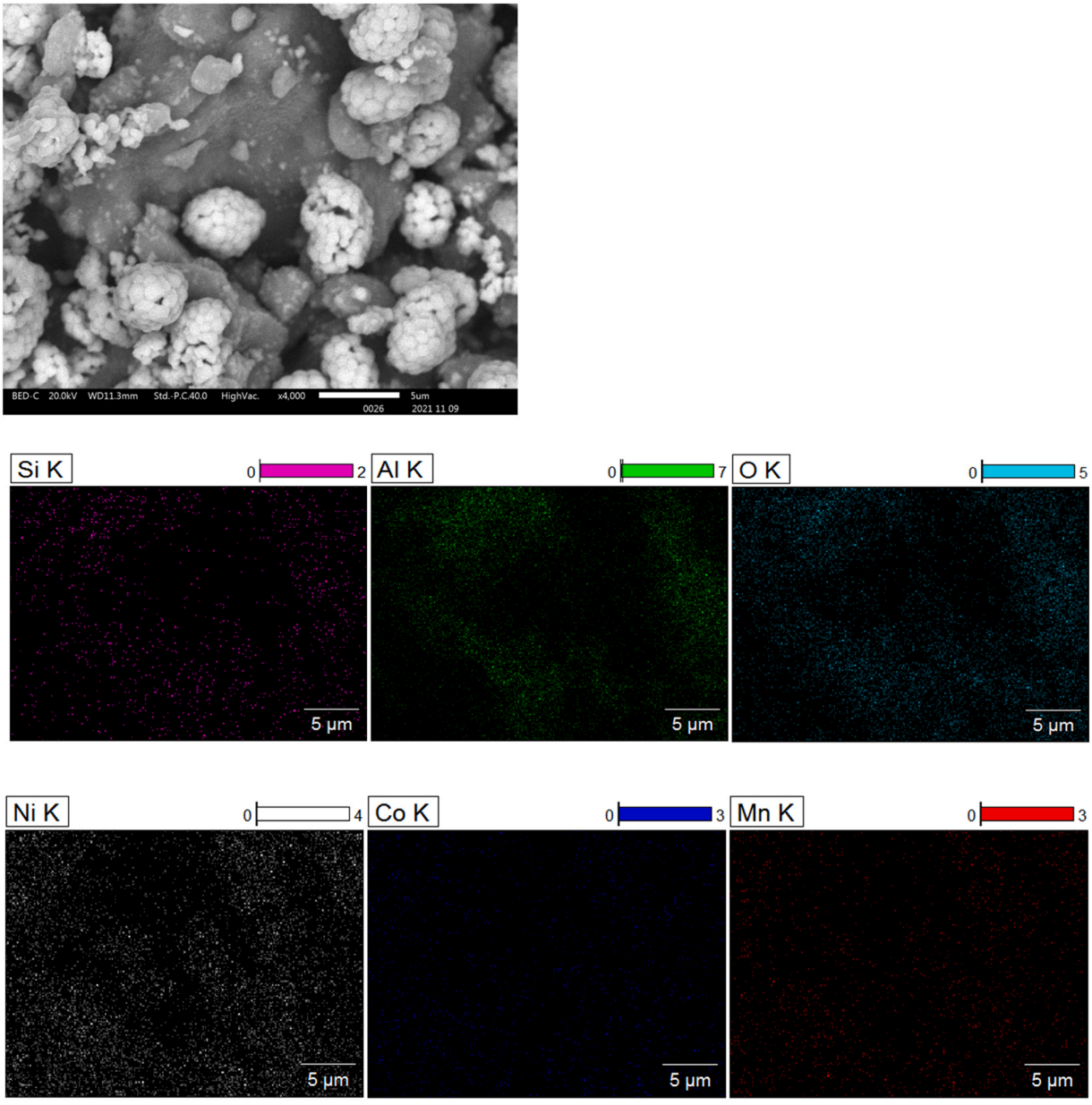

Fig. 7. EDS images of between the LCNM precursor and the mullite sample after heat treatments at 950 °C for 10 h.

were severely corroded by LNCM. However, the CA_6 sample was only slightly corroded.

(3) The corrosion resistance of mullite was better than that of bubble alumina. Moreover, the CA_6 had the best corrosion resistance amongst the three insulating refractories, which is conducive to the application of high temperature kilns in lithium battery industry.

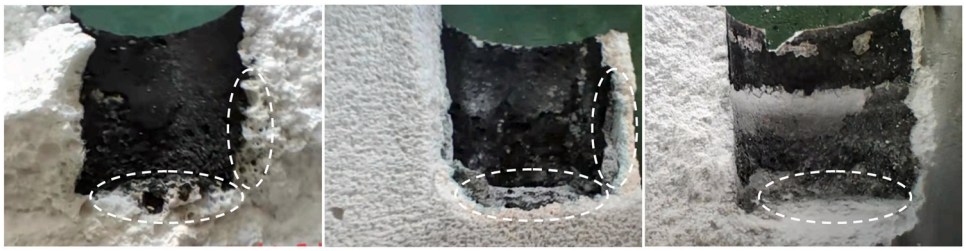

Fig. 8. Macrograph view for the section of the insulating refractory after 10 times of corrosion: (a) bubble alumina, (b) mullite and (c) CA_6 samples.

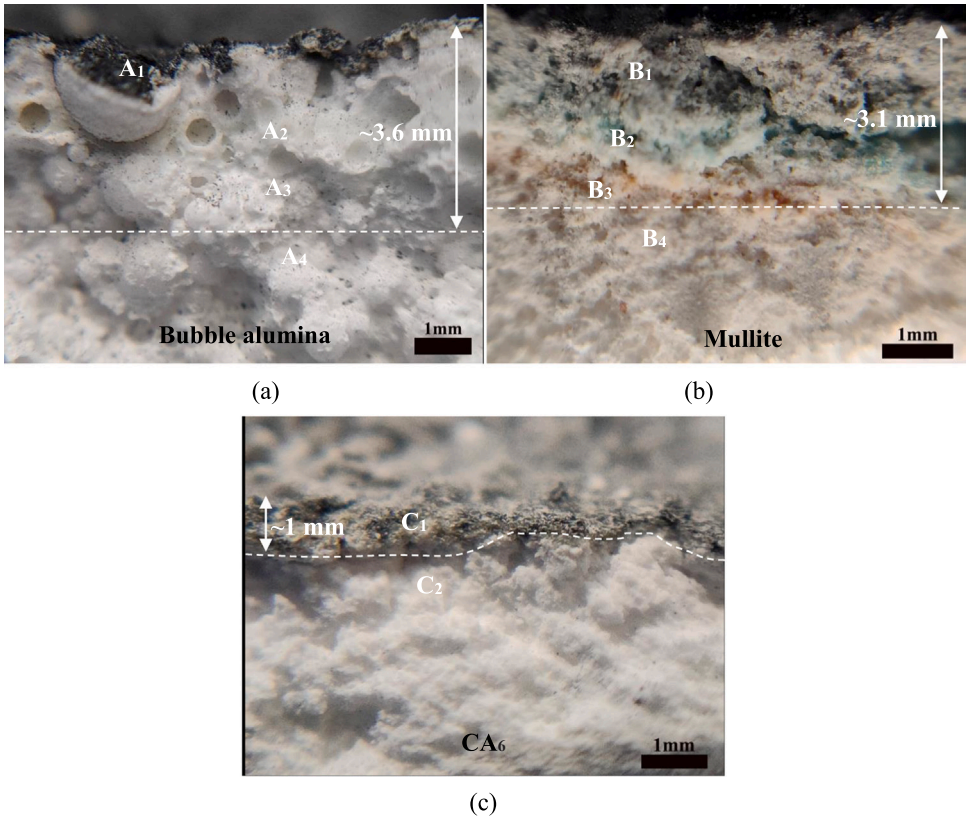

Fig. 9. Section colour view of the reaction layer at the bottom of the samples: (a) bubble alumina, (b) mullite and (c) CA_6 samples.

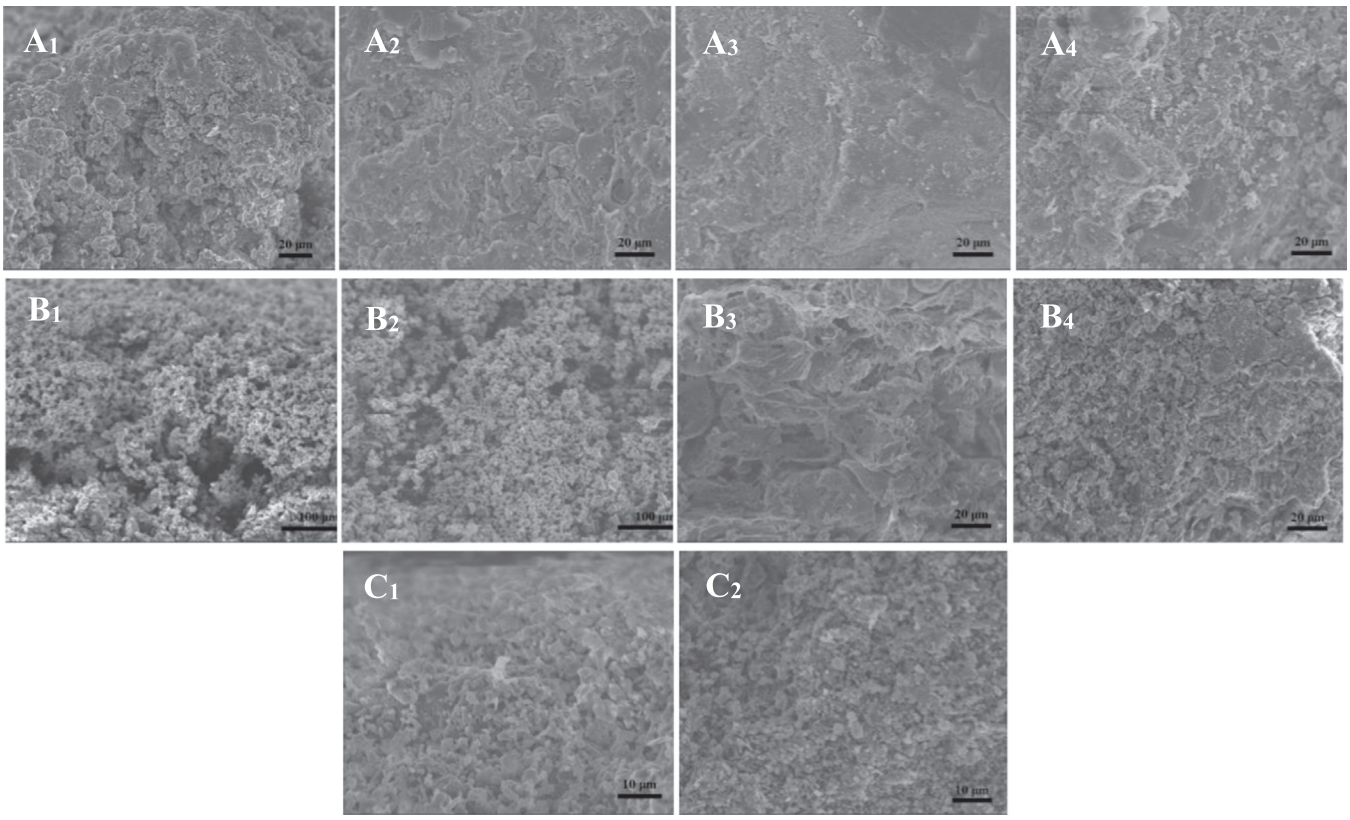

Fig. 10. SEM observation for the different sectional areas of the insulating refractories after 10 times of corrosion showed in Fig. 9.

CRediT authorship contribution statement

Bo Yin: Conceptualization, Methodology, Software, Data curation, Writing – original draft. **Yuanbing Li:** Writing – review & editing. **Shun Wang:** Supervision, Validation. **Yifeng Zheng:** Investigation.

Data availability

Data will be made available on request.

Declaration of Competing Interest

The authors declare that they have no known competing financial interests or personal relationships that could have appeared to influence the work reported in this paper.

Acknowledgement

This work was supported by National Natural Science Foundation of China (No. 21978133).

References

[1] Y. Chen, Q. He, Y. Mo, W. Zhou, Y. Zhao, N. Piao, C. Liu, P. Xiao, H. Liu, B. Li, S. Chen, L. Wang, X. He, L. Xing, J. Liu, Engineering an insoluble cathode electrolyte interphase enabling high performance NCM811//graphite pouch cell at 60 °C, Adv. Energy Mater. 12 (33) (2022) 2201631.

[2] D. Yan, Y.V. Lim, G.Z. Wang, Y. Shang, X.L. Li, D.L. Fang, M.E. Pam, S.A. Yang, Y. Wang, Y.M. Shi, H.Y. Yang, Unlocking rapid and robust sodium storage performance of zinc-based sulfide via indium incorporation, ACS Nano 15 (2021) 8507–8516.

[3] J. Wang, Q. Yuan, Z. Ren, C. Sun, J. Zhang, R. Wang, M. Qian, Q. Shi, R. Shao, D. Mu, Y. Su, J. Xie, F. Wu, G. Tan, Thermochemical cyclization constructs bridged dual-coating of Ni-rich layered oxide cathodes for high-energy Li-ion batteries, Nano Lett. 22 (13) (2022) 5221–5229.

[4] Q. Lu, C. Wang, D. Bao, H. Duan, F. Zhao, K.D. Davis, Q. Zhang, R. Wang, S. Zhao, J. Wang, H. Huang, X. Sun, High-performance Quasi-solid-state pouch cells enabled by in-situ solidification of a novel polymer electrolyte (n/a (n/a)), Energy Environ. Mater. (2022), https://doi.org/10.1002/eem2.12447

[5] Y.T. Xu, J.J. Zhu, J.Z. Feng, Y. Wang, X.X. Wu, P.J. Ma, X. Zhang, G.Z. Wang, X.B. Yan, A rechargeable aqueous zinc/sodium manganese oxides battery with robust performance enabled by Na_2SO_4 electrolyte additive, Energy Storage Mater. 38 (2021) 299–308.

[6] E.C. Lee, J. Park, Unraveling the Structural Instability of $Li(Ni_{0.80}Co_{0.15}Al_{0.05})O_2$ as a Cathode Material Due to Operating a Li-ion Battery, Small 18 (25) (2022) 2200581.

[7] H. Pegel, O. von Kessel, P. Heugel, T. Deich, J. Tübke, K.P. Birke, D.U. Sauer, Volume and thickness change of NMC811|SiOx-graphite large-format lithium-ion cells: from pouch cell to active material level, J. Power Sources 537 (2022) 231443.

[8] N. Yabuuchi, T. Ohzuku, Novel lithium insertion material of LiCo1/3Ni1/3Mn1/$3O_2$ for advanced lithium-ion batteries, J. Power Sources 119–121 (2003) 171–174.

[9] H. Liang, Z. Wang, H. Guo, J. Wang, J. Leng, Improvement in the electrochemical performance of $LiNi_{0.8}Co_{0.1}Mn_{0.1}O_2$ cathode material by Li_2ZrO_3 coating, Appl. Surf. Sci. 423 (2017) 1045–1053.

[10] M. Zhang, J. Shen, J. Li, D. Zhang, Y. Yan, Y. Huang, Z. Li, Effect of micron sized particle on the electrochemical properties of nickel-rich $LiNi_{0.8}Co_{0.1}Mn_{0.1}O_2$ cathode materials, Ceram. Int. 46 (4) (2020) 4643–4651.

[11] D. Ren, Y. Yang, L. Shen, R. Zeng, H.D. Abruña, Ni-rich $LiNi_{0.88}Mn_{0.06}Co_{0.06}O_2$ cathode interwoven by carbon fiber with improved rate capability and stability, J. Power Sources 447 (2020) 227344.

[12] N. Chen, B. Li, W. Gui, S. Xu, J. Wang, J. Dai, Research on temperature field change trend of the sintering process for lithium-ion battery cathode materials, IFAC Pap. 51 (21) (2018) 307–312.

[13] G. Cheng, T. Zhao, Y. Zhao, T. Jia, Y. Li, X. Wang, C. Dong, Wetting, cladding and corrosion properties of alkaline slag on dense corundum refractories, Ceram. Int. 48 (4) (2022) 5795–5804.

[14] Y. Gao, H. Zhang, Q. Wang, G. Li, Effect of applied voltage on wetting and corrosion of corundum refractory by $CaO–SiO_2–MgO$ molten slag, Ceram. Int. 48 (7) (2022) 9753–9764.

[15] L. Xu, D. Zhang, Y. Liu, M. Chen, N. Wang, Comparison of microstructure, thermomechanical property and corrosion resistance of bauxite-corundum refractory castables reinforced by two approaches, Ceram. Int. 47 (10, Part A) (2021) 13660–13668.

[16] S. Wang, Q. Guo, Y. Gong, S. Liao, L. Bao, G. Yu, Corrosion in high alumina refractory serviced in a bench-scale entrained flow gasifier, Ceram. Int. 47 (2) (2021) 2214–2221.

[17] Y. Zhang, L. Sun, Y. Lei, W. Ma, Z. Li, Corrosion behavior of carbon, Al_2O_3, and MgO refractories during the preparation of a Ti–Si–Al alloy via the aluminothermic reduction of a Ti-bearing blast-furnace slag, Ceram. Int. 47 (13) (2021) 18044–18052.

[18] B. Ma, C. Su, X. Ren, Z. Gao, F. Qian, W. Yang, G. Liu, H. Li, J. Yu, Q. Zhu, Preparation and properties of porous mullite ceramics with high-closed porosity and high strength from fly ash via reaction synthesis process, J. Alloy. Compd. 803 (2019) 981–991.

[19] D. Ding, G. Ye, L. Chen, Superior corrosion resistance $KAlSi_2O_6$-containing materials for calcining Li-ion battery cathode materials, Corros. Sci. 157 (2019) 324–330.

[20] L.M.M. Costa, J. Sakihama, R. Salomão, Characterization of porous calcium hexaluminate ceramics produced from calcined alumina and microspheres of Vaterite (μ-$CaCO_3$), J. Eur. Ceram. Soc. 38 (15) (2018) 5208–5218.

[21] J. Chen, H. Chen, W. Mi, Z. Cao, B. Li, C. Liang, Substitution of Ba for Ca in the Structure of $CaAl_{12}O_{19}$, J. Am. Ceram. Soc. 100 (1) (2017) 413–418.

[22] X. Duan, H. Zheng, Y. Chen, F. Qian, G. Liu, X. Wang, Y. Si, Study on the corrosion resistance of cordierite-mullite and SiC refractories to Li-ion ternary cathode materials, Ceram. Int. 46 (3) (2020) 2829–2835.

[23] H. Schneider, R.X. Fischer, J. Schreuer, Mullite: crystal structure and related properties, J. Am. Ceram. Soc. 98 (10) (2015) 2948–2967.

[24] R. Xiang, Y. Li, S. Li, Z. Xue, Z. He, L. Wang, H. Wang, Corrosion degradation of mullite subject to carbon monoxide atmosphere at 1000°C–1600°C, Int. J. Appl. Ceram. Technol. 17 (4) (2020) 1688–1692.

[25] P. Zhai, L. Chen, Y. Yin, S. Li, D. Ding, G. Ye, Interactions between mullite saggar refractories and Li-ion battery cathode materials during calcination, J. Eur. Ceram. Soc. 38 (4) (2018) 2145–2151.

[26] D. Ding, L. Chen, G. Liao, L. Zheng, S. Gao, G. Ye, Preparation of andalusite-corundum-$KAlSi_2O_6$ material for the calcination of Li-ion battery cathode materials, J. Alloy. Compd. 798 (2019) 367–374.

[27] H. Wang, Y. Li, S. Li, R. Xiang, l Han, S. Li, Z. Zhou, Corrosion of Li-ion battery cathode materials on mullite insulation materials during calcination, Ceram. Int. 48 (14) (2022) 20220-20227.

[28] C.-H. Jo, N. Voronina, S.-T. Myung, Single-crystalline particle Ni-based cathode materials for lithium-ion batteries: strategies, status, and challenges to improve energy density and cyclability, Energy Storage Mater. 51 (2022) 568–587.

[29] N.-Y. Park, G.-T. Park, S.-B. Kim, W. Jung, B.-C. Park, Y.-K. Sun, Degradation mechanism of Ni-Rich cathode materials: focusing on particle interior, ACS Energy Lett. 7 (7) (2022) 2362–2369.

[30] Z. Ahaliabadeh, X. Kong, E. Fedorovskaya, T. Kallio, Extensive comparison of doping and coating strategies for Ni-rich positive electrode materials, J. Power Sources 540 (2022) 231633.

[31] Y. Li, R. Xiang, N. Xu, Q. Wang, S. Li, M. Wu, C. Yang, Fabrication of calcium hexaluminate-based porous ceramic with microsilica addition, Int. J. Appl. Ceram. Technol. 15 (4) (2018) 1054–1059.

[32] J. Zhu, J. Zheng, G. Cao, Y. Li, Y. Zhou, S. Deng, C. Hai, Flux-free synthesis of single-crystal $LiNi_{0.8}Co_{0.1}Mn_{0.1}O_2$ boosts its electrochemical performance in lithium batteries, J. Power Sources 464 (2020) 228207.

[33] S.-I. Hirano, T. Hayashi, T. Kageyama, Synthesis of $LiAlO_2$ powder by hydrolysis of metal alkoxides, J. Am. Ceram. Soc. 70 (3) (1987) 171–174.